FAST TRACK PAPER

Resolving crustal thickness using SS waveform stacks

Catherine A. Rychert* and Peter M. Shearer

Institute of Geophysics and Planetary Physics, Scripps Institution of Oceanography, University of California, San Diego, 9500 Gilman Drive M/C 0225, La Jolla, CA 92093, USA. E-mail: glcar@bristol.ac.uk

SUMMARY

We image lithospheric interfaces using variations in the character of SS waveform stacks, a method we term SS Lithospheric Interface Profiling (SSLIP). The variations are caused by reflected phases, that is, underside reflections (SS precursors) and topside multiples (SS reverberations), created at velocity discontinuities near the midpoint of the SS ray path. Stacks from continental versus oceanic bounce point regions produce distinctly different SS waveforms, consistent with the large continent/ocean difference in crustal thickness. To investigate the potential of SS waveform stacks to constrain Moho depths under continents, we develop a method to fit continental bounce point stacks with a reference SS waveform convolved with a crustal operator. The SSLIP inferred Moho depths agree with the CRUST 2.0 model in Asia for those regions where the SS bounce point density is the highest. The SSLIP depths are correlated (correlation coefficient 0.82) with the CRUST 2.0 values averaged over sample bins of 10° radius. The SSLIP method has broad lateral resolution in comparison to most other methods for resolving crustal thickness, but has the potential to sample regions where station coverage may be sparse.

Key words: Body waves; Crustal structure; Asia.

GJI Seismology

INTRODUCTION

Many questions remain regarding the formation of the continents, mantle dynamics, and planetary evolution. Some of these may be better understood by constraining the structure of the plates, and thus the imaging of lithospheric seismic velocity discontinuities. Perhaps the most fundamental lithospheric discontinuity globally is the Moho, which was discovered 100 yr ago in Croatia by seismologist Andrija Mohorvičić by studying passive source arrivals at various epicentral distances (Mohorovičić 1910; Grad *et al.* 2009). This discontinuity has since been widely mapped using a variety of geophysical, geochemical, and geological constraints, and it is well established that it represents the compositional change distinguishing the crust from the mantle. The Moho is characterized by a sharp impedance change, with *P* and *S* velocity jumps of 15–20 per cent, and thus seismic imaging using a variety of techniques is a powerful means of mapping its depth. Moho depths vary from ∼6–8 km beneath oceans to 20–75 km beneath continents, where it is deeper beneath orogens and shallower beneath rifts (Christensen & Mooney 1998). However, depth variations are sometimes more complicated and/or abrupt (e.g. Zhu & Helmberger 1998; Zhang *et al.* 2009) owing to the long and complicated history of the continental crust.

An accurate model of Moho depth is important for a variety of reasons, both directly impacting our understanding of fundamental lithospheric processes, and also influencing our ability to seismically image other features. For instance, Moho depth has a significant impact on surface wave inversions for upper mantle seismic structure (Zhou *et al.* 2005) and the ability to accurately locate nuclear explosions and earthquakes (Oda & Ushio 2007; Priestly *et al.* 2008). Moho depth can also impact the accuracy of receiver-function imaging of deeper discontinuities (e.g. Rychert *et al.* 2007; Rychert & Shearer 2009).

Seismic resolution of the depth to the Moho is dependent on the dominant period of the waveform, the way the waveform interacts with the boundary, that is, scattering versus transmission, and the degree of trade-off between crustal thickness and velocity (Bostock & Rondenay 1999; Zhu & Kanamori 2000; Rychert *et al.* 2007). The Moho is sharp, and it may be imaged using high-frequency scattered waveforms. Therefore, reflection imaging provides the highest depth resolution, although generally local in scale. Refraction imaging also provides high resolution over larger swaths. Many studies have used these active source methods (using chemical or nuclear explosions) to measure Moho depths (e.g. MONA-LISA

*Now at: Department of Earth Sciences, University of Bristol, Wills Memorial Building, Queen's Road, BRISTOL BS8 1RJ, United Kingdom.

Working Group 1997; Steer *et al.* 1998; Morozova *et al.* 1999; Morozova *et al.* 2000; Pavlenkova *et al.* 2002). Active source results usually provide sensitivity to *P* velocity, given the waveforms that are considered, though *S* velocities may also be used (e.g. Behm 2009).

Ps and Sp receiver functions give relatively high resolution of Moho depth without the need for active source experiments, though lateral resolution is still limited to a small cone beneath the locations of seismic stations (e.g. Bostock 1998; Bump & Sheehan 1998; Zhu & Kanamori 2000; Rychert *et al.* 2005; Chen *et al.* 2006; Kumar *et al.* 2006; Oreshin *et al.* 2008; Ozacar *et al.* 2008; Schutt *et al.* 2008; Hansen & Dueker 2009). These waveforms are sensitive to sharp changes in shear wave velocity. Moho depth resolution may suffer from a trade-off between crustal velocity and Moho depth, but considering the moveout of crustal reverberations can minimize this trade-off (e.g. Zhu & Kanamori 2000; Rychert *et al.* 2005).

Results from these three high-frequency methods, reflection, refraction, and receiver functions have been synthesized into a widely known global model, CRUST 2.0, which uses statistical interpolations in regions without data (Mooney *et al.* 1998; Bassin *et al.* 2000). This model is particularly useful in regions where high resolution is available, that is, zones where active source experiments have been performed or permanent seismic stations or temporary arrays have been analysed with receiver function methods. However, because many of these high-resolution studies are necessarily local or regional in scale and mostly located on continents, some areas are poorly constrained, for example, the oceans (e.g. Rychert *et al.* 2009).

Surface waves constrain lithospheric velocities over wide swaths, but generally do not have the resolution to image sharp features such as the Moho. However, because they have the potential to provide global coverage, attempts have been made to use surface waves to constrain the boundary, both with Monte Carlo (model CUB2) and neural network inversion schemes (model MDN) (Shapiro & Ritzwoller 2002; Meier *et al.* 2007). Both studies use CRUST 2.0 as a starting model, one damping depths to within 5 km of the starting model (Shapiro & Ritzwoller 2002). These studies are in general agreement, but discrepancies still exist (Meier *et al.* 2007), and complete global coverage at high resolution has yet to be obtained.

SS precursors can also be used to image upper-mantle discontinuity structure (e.g. Flanagan & Shearer 1998; Deuss & Woodhouse 2001; Gu & Dziewonski 2002; Lawrence & Shearer 2008). SS precursors have the advantage of resolving discontinuities in regions far away from seismic stations since they are sensitive to structure at the SS bounce point, that is, roughly the midpoint between source and receiver. In this way SS precursors have provided global constraints on transition zone discontinuities.

However, SS precursors are generally observed at longer periods than receiver functions and their broader pulse widths cannot resolve fine-scale discontinuity structure or closely spaced interfaces. For this reason, underside Moho reflections do not appear as a distinct phase in SS precursor studies. However, Moho structure does affect the character of the stacked SS waveform, and here we demonstrate that this variation may be exploited to constrain lithospheric structure, in particular the depth to the Moho using a crustal operator technique (Shearer 1996). Because of the size of the SS bounce point Fresnel zone and the large number of waveforms required to resolve the relatively subtle waveform features that may be translated to Moho depth, this method has wide lateral resolution. Its potential utility lies in its ability to sample structure in regions with sparse station coverage.

DATA AND STACKING METHOD

We used the global IRIS FARM data set from 1990 to 2007 with event-to-station distances of 90° to 140° preprocessed to remove the instrument response. Station locations are shown in Fig. 1. The 140° cut-off is to avoid contamination from ScSScS, which arrives closely following SS at longer distances. We restricted source depths to 0–75 km to minimize complications from depth phases. We rotated the horizontal components to obtain the transverse component, which we then Hilbert transformed to remove the expected Hilbert transform of the SS phase and produce more symmetric pulses. Following low-pass filtering at 0.1 Hz, we aligned the waveforms on the maximum amplitude (positive or negative) in a window 10 s before and 40 s after the theoretical SS arrival time, normalizing to unit amplitude and flipping the polarity of the negative pulses before stacking. We calculated the signal-to-noise ratio for each waveform using the standard deviation in a window 255 s to 5 s before the SS peak to the subsequent 30 s window, and rejected waveforms with signal-to-noise ratios less than three. We obtained 261 686 waveforms that fit the source parameters described above, and 113 975 of these waveforms also fit the signal-to-noise criterion (Fig. 2). We weighted the stacked waveforms according to their signal-to-noise ratio to a maximum weight of eight before stacking, and normalized the final stacks to unit amplitude.

CONTINENT–OCEAN DIFFERENCES

We divided SS waveforms by bounce point location into separate continental (red circles in Fig. 2) and oceanic (blue circles in Fig. 2) bins, using the tectonic regionalization of Jordan (1981). The resulting stacked waveforms have distinctly different shapes (Fig. 3). The oceanic stack (solid line in Fig. 3) is closer to a symmetric pulse. The continental stack (dashed line in Fig. 3) has a more asymmetric shape, with a lower amplitude negative sidelobe on its leading side and a higher amplitude negative sidelobe on its trailing side. As we discuss later, this is caused by the filtering effect of a thicker continental crust on the SS reflections.

We also examined waveform stacks at a finer spatial scale to map regional variations in Moho depth. We used SS bounce point bins of 10° radius, spaced about 10° apart. There is some overlap between adjacent bins, and an individual waveform may be used in multiple bins. We compared these 10° waveform stacks to the continental and oceanic global stacks of Fig. 3 by computing correlation coefficients between each 10° stack and the two global stacks, using a signal window 60 s before and after the SS peak. We then compared the sizes of the continental and oceanic correlation coefficients in each bin to determine the most likely type of crust. The results of this simple continent–ocean discriminant are shown in Fig. 4. Green circles indicate bins that correlate more strongly with the continental reference waveform stack, whereas blue circles indicate bins that correlate better with the oceanic stack. Because the bounce point distribution within each bin is not necessarily uniform, the results are plotted at the average bounce point location of the bin, the bin centroid. This is the reason that the circle locations are not equidistant in Fig. 4.

Bins that are more correlated with the global continental SS stack generally correspond to continental locations, and those that are more correlated with the global oceanic stack are found in oceanic locations, with only a few exceptions (Fig. 4). This continent–ocean discriminator can be compared with the oceanic/continental labels in the coarse (5° × 5° cell) tectonic regionalization of Jordan (1981).
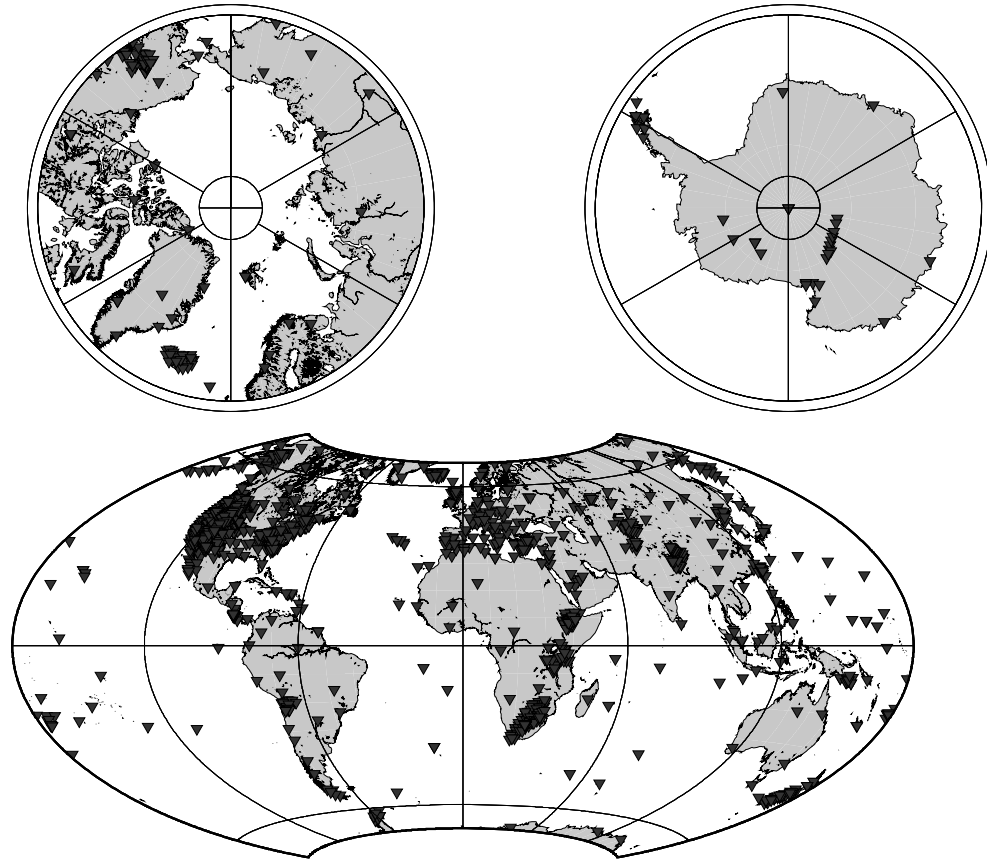
Figure 1. Station map. Grey inverted triangles indicate stations that recorded SS waveforms exceeding the signal-to-noise ratio cut-off (3) that were used in this study.

Our SS result agrees with the Jordan (1981) model at the location of the bin centroids for 82 per cent of the bins, more specifically 94 per cent of oceanic bins and 61 per cent of continental bins. The largest discrepancy, the apparent oceanic SS behaviour in northeast Africa, occurs in an area of relatively low bounce point density (compare Figs 2 and 4). The same is true for the few remaining discrepancies, for example, bin 303 in Australia and bins 201, 202 and 338 in the Pacific. Generally bins that produce discrepancies are near the ocean–continent boundary and/or have low bounce point density, <500 waveforms per stack.

We tested the sensitivity of these results to differences in the low-pass filter (checking values of 0.05, 0.075, 0.1, 0.15, 0.25, 0.5 and 1.0 Hz) and obtained very similar outcomes for the ocean–continent discrimination test. The results plotted in Fig. 4 changed in less than 5 per cent of the bins, even when we used extreme low-pass filters.

INVERSION METHOD: CONCEPT AND APPLICATION

The majority of the observed variation in SS character between the continent and ocean bins in Fig. 3 is likely caused by reflections off the Moho, which is the strongest velocity discontinuity in the lithosphere. The oceanic crust is much thinner than the continental crust (∼6–8 km versus ∼25–75 km). Velocity discontinuities such as the Moho create two first-order SS reflections, one that arrives before and one that arrives after the SS phase. We neglect second-

and higher-order reflections, which are much smaller in amplitude. The arrival times of the precursor and reverberated phase relative to SS are related to the two-way traveltime between the discontinuity and the surface. The polarities of the phases are dependent on the reflection coefficient of the interface. For a velocity increase with depth, such as the Moho, the bottom-side reflection, the SS precursor, arrives before the SS phase with positive polarity. The SS reverberation, which reflects twice off the free surface and once off the top of the Moho, arrives after the SS phase with negative amplitude (Fig. 5). Assuming the plane-wave approximation that the secondary phases have the same ray parameter as the main phase (reasonably accurate for the Moho but not for deeper discontinuities such as at 410 km) and a uniform crustal layer, the traveltime offset is given by the layer delay time:

$$\tau = 2h\sqrt{1/\beta^2 - p^2}, \tag{1}$$

where p is the ray parameter, h is the crustal thickness and β is the shear velocity of the crust. Compared to direct SS, the underside Moho reflection arrives early by this time, the Moho reverberation arrives delayed by this time. For the modelling presented here, we assume $\beta = 3.55$ km s^{-1}, based on the CRUST 2.0 and MDN crustal velocities averaged over the region covered by our 10° bins in Asia, 3.54 km s^{-1} and 3.57 km s^{-1}, respectively. We assume $p = 0.12$ s km^{-1}, the global average slowness for the SS data that we analyse.

A simple crustal operator may be used to approximate the effects of Moho structure on the SS waveform stacks (Shearer 1996). A
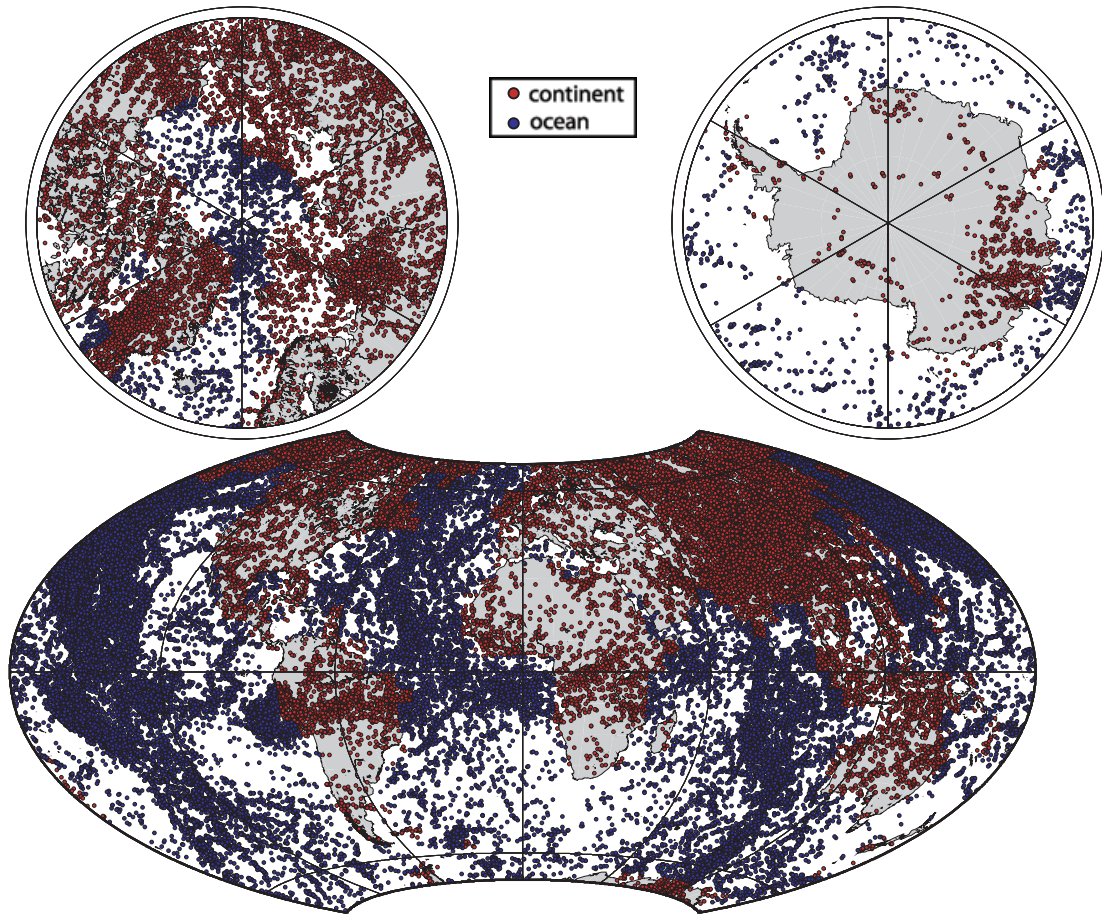
Figure 2. SS bounce point distribution. Red and blue circles indicate continental and oceanic SS bounce points, respectively. Bounce points are shown only for waveforms that passed the source parameter criterion and the signal-to-noise ratio cut-off of three, as described in the text. The continent–ocean distinction here is based in the tectonic regionalization of Jordan (1981).

crustal operator convolved with a reference SS waveform, that is, one not affected by thick crustal structure, gives the waveform observed for continental bounce points (Fig. 5). Similarly, an inverse crustal operator convolved with the continental stack results in the original reference waveform (a simple first-order approximation to the inverse operator is shown in Fig. 5).

The Moho is a relatively shallow discontinuity, and thus its associated precursors and reverberations arrive close to the SS phase, especially for the oceanic crust. A reference pulse convolved with a crustal operator corresponding to typical oceanic crust (6–8 km thick) is relatively unaffected by the convolution (Shearer 1996) because the arrival times of the phases are so close. This is the reason that oceanic SS stacks are relatively symmetric in comparison to continental stacks (Fig. 3). This also means that SS precursors do not have the ability to constrain oceanic crustal thicknesses, or any relatively thin crust. However, in the case of the continents, the thicker crust means that the precursors and reverberations arrive at greater time differentials from the SS phase. The resulting SS stack has a distinct asymmetry, and the potential to constrain Moho depths.

We should note at this point that asymmetric pulses are often seen in waveforms from single events, because of interference with depth phases. However, stacks of enough of these sources (created by aligning waveforms on their maximum amplitudes) nonetheless will produce a repeatable source–time function because these differences tend to cancel out (e.g. Shearer 1991). Our method
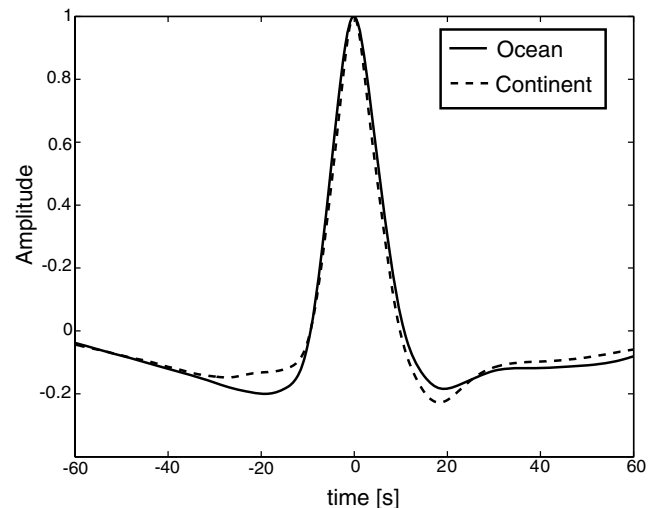

Figure 3. Global ocean versus continent stacks. The global SS waveform stack of oceanic bounce points (solid line) is compared to the global SS waveform stack of continental bounce points (dashed line).

works because we process enough data that the waveform stacks become very consistent in shape, but our results do become less reliable when we consider bounce point bins with smaller numbers of waveforms.
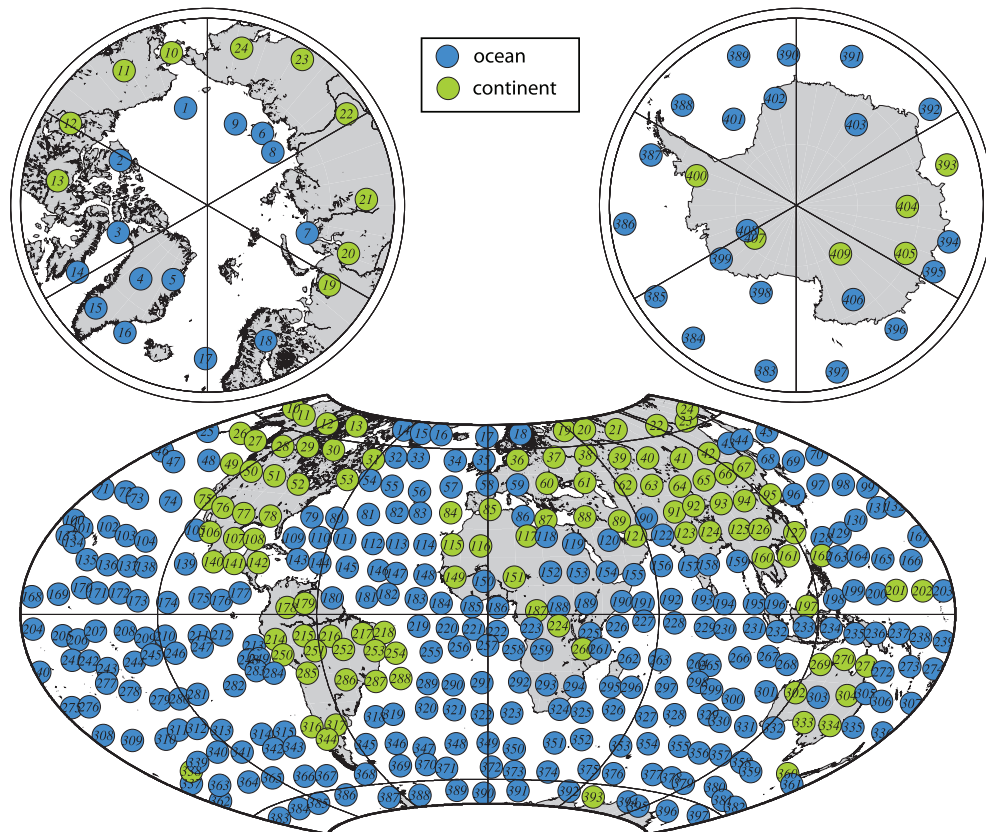
Figure 4. Result of the continent–ocean binary test. Each circle corresponds to the location of a common bounce point bin, spaced at regular 10° intervals, but plotted at the average bounce point location, the bin centroid. The colour of the circle is related to the correlation coefficients of the waveform stacks of the 10° bins with the global continent and ocean stacks in Fig. 2. Green circles indicate bins that are more correlated with the continental global stack. Blue circles show bins that are more correlated with the oceanic global stack. The numbers printed within the coloured circles correspond to the bin numbers of our naming scheme, starting with bin 1 at the North Pole, and continuing to bin 409 at the South Pole.

To model our results, we convolved a reference stack with forward crustal operators corresponding to a variety of Moho structures. We used the global oceanic stack as a reference since it is relatively unaffected by crustal structure. However, we also performed tests with alternate reference phases and obtained similar results, as described in a later section. We determined Moho depth for the continental waveform stacks (green circles in Fig. 4) using a grid search approach. We experimented with both one-parameter (Moho depth) and three-parameter (Moho depth, impedance contrast, and sharpness) inversions. The three parameters correspond to crustal operators with precursor and reverberation variations in timing, amplitude and Gaussian spread function, respectively. In the one-parameter inversions, a delta function is assumed, and amplitude is fixed to its best-fitting global average.

SSLIP MOHO DEPTH RESULTS

We focus our discussion on the SSLIP inversion results in Asia where resolution is best owing to the dense bounce point coverage (Fig. 2). Waveform stacks from Asia contain between 482 (bin 89) and 3912 (bin 66) individual waveforms. Examples of some of the best-fitting convolved waveforms and the SS data stacks are shown in Fig. 6, together with the global oceanic reference stack. The inversions produce 54 and 65 per cent decreases in variance over the oceanic reference model for the one-parameter and three-parameter models, respectively.

Our Moho depth estimates from the one-parameter inversions are shown in Fig. 7. Bin locations are plotted at the average bounce point location within each bin. Only bins of continental character (as determined by the correlation coefficient test) are plotted, given that the SSLIP method cannot resolve very shallow Moho depths. Continental SSLIP Moho depths beneath Asia (generally 26–55 km) are consistent with the typical range of crustal thicknesses in Asia (e.g. Bassin *et al.* 2000; Shapiro & Ritzwoller 2002; Liu *et al.* 2006; Meier *et al.* 2007; Zhang & Wang 2007). In addition SSLIP crustal thickness estimates increase from the edges of the continent toward the Himalayan Mountains and the Tibetan Plateau, as is expected for continental margins and orogenies.

ERROR ANALYSIS

Our solution from the grid search is the model with the smallest residual. Multiple minima do not exist, since the shapes of the crustal thickness versus residual curves generally appear well-behaved with singular well-defined minima. Although residuals are slightly reduced by including amplitude and spread parameters, an *F*-test for significance of regression indicates that these parameters are not significantly resolved. However, since the trade-off in the effects of these model parameters on crustal thickness is minimal there is little difference in the resulting Moho depths. Moho depth results for inversions assuming one-parameter, that is, those with the spread-function fixed as a delta function and amplitude fixed at the
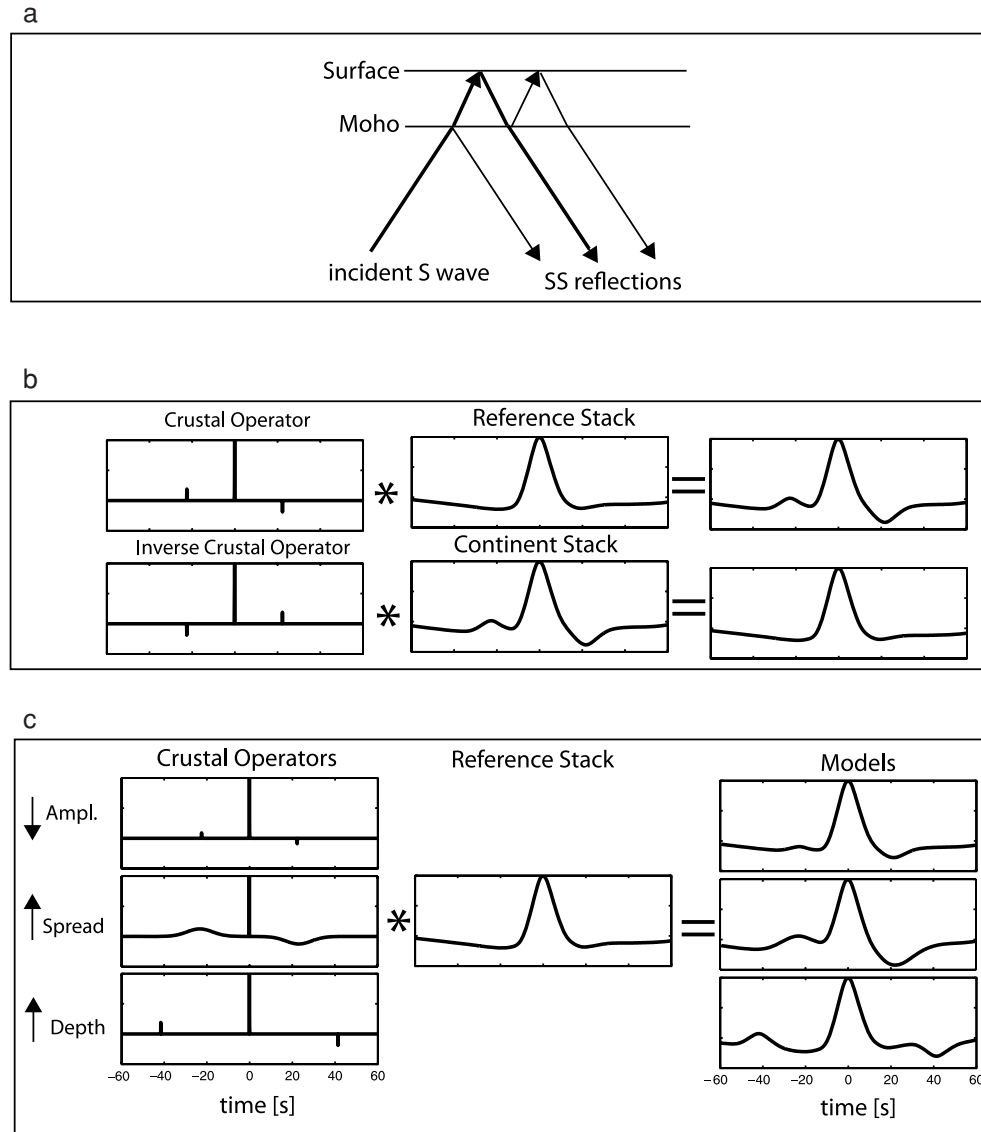
Figure 5. Schematic of the forward model. (a) Ray paths of the direct SS waveform as well as the SS precursor and reverberation near the bounce point. (b) The data may be described as a crustal operator convolved with a reference stack (top row). An inverse crustal operator (approximation) convolved with a continental SS stack results in the original reference phase (bottom row). (c) The effects of variations in the crustal operator parameters (in comparison to the model shown in b) are demonstrated, that is, decreased amplitude (top row), increased spread function (middle row), and increased Moho depth (bottom row). Note that the vertical axis of the crustal operator in the spread function example is not to scale, since the waveform has been enlarged for viewing purposes.

global average, were very close to those assuming three-parameter inversions, within estimated errors. The Moho depth map (Fig. 7) is very close for the two cases.

To quantify error we performed a bootstrap test for each of the 10° waveform stacks in Asia. We stacked the same number of waveforms that were originally in the bin, randomly resampling the waveforms included in the stack. We then inverted the resampled stack for the best-fitting model. We performed this bootstrap test 100 times for each bin and estimated standard errors from the resulting depth distributions. These one-standard-error estimates were generally 0.5–4 km, though, as expected, larger errors occur for those bins with smaller numbers of data (Figs 8 and 9). Therefore, 95 per cent error limits for Moho depths across the region are generally no more than ±8 km. Modelling assumptions such as ray parameter

and shear velocity also contribute to uncertainty, but on a much smaller scale.

DISCUSSION

We compare the SSLIP Moho depth results to crustal thicknesses in the CRUST 2.0 model (Bassin *et al.* 2000) and the MDN model (Meier *et al.* 2007), both of which are specified on a 2° × 2° grid. CRUST 2.0 is a compilation of reflection, refraction, and receiver function studies with statistical inferences in unsampled regions (Bassin *et al.* 2000). The MDN model constrains Moho depth using a surface wave inversion, where CRUST 2.0 is the starting model (Meier *et al.* 2007). We did not do a direct
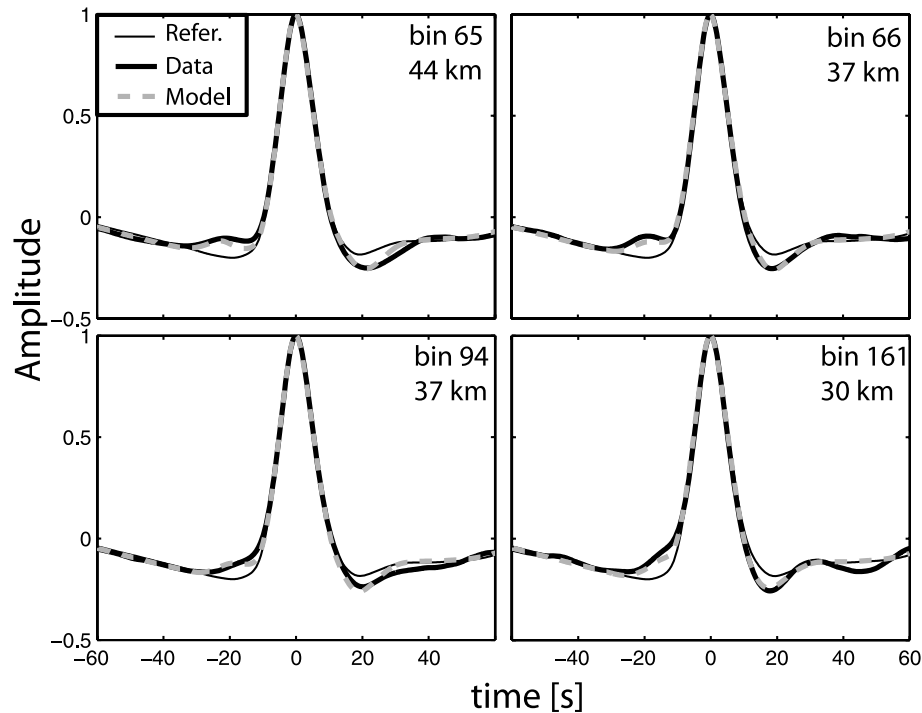
Figure 6. Examples of the waveform fits in Asia. SS waveform stacks (thick black lines) are plotted with waveforms corresponding to the best-fitting model (dashed gray lines). The oceanic reference stack is also plotted (thin black lines) to demonstrate the improvement in fit. The numbers in each box indicate bin number and the best-fitting crustal thickness from the one-parameter inversion, that is, amplitude and Gaussian spread parameters fixed.

comparison to model CUB2 (Shapiro & Ritzwoller 2002), another surface wave model, since its Moho depths are generally very close to CRUST 2.0, damped within 5 km, and our resolution is likely lower than that.

Crustal thicknesses increase from the edges of the Asian continent toward the Himalayan orogeny in all models. The magnitudes of the SSLIP Moho depths are also in general agreement with those of CRUST 2.0 and MDN (Fig. 7). All models reach global maxima beneath Tibet, and the locations of these maximum values are in general agreement, somewhere between 31°–33° N and 83°–98° W. The maximum crustal depths of the models are 75, 79 and 55 km for model CRUST 2.0, MDN and the SSLIP models, respectively. The Moho is deepest in the MDN model (79 km), and it is deep (75 km) over a wider area in the CRUST 2.0 model, while it is relatively shallow in the SSLIP model (Fig. 7). The shallow SSLIP value is likely owing to lateral averaging in SSLIP, that is, the fact that the method has generally lower spatial resolution. CRUST 2.0 and MDN generally have much better resolution than SSLIP across the region.

We tested the ability of the SSLIP method to resolve deeper crust beneath Tibet. We performed stacks of data in a bin centred near the deep Moho of model CRUST 2.0 (latitude = 33° N, longitude = 85° E). We included waveforms with bounce points at radii up to 2° and also 3° away from the bin center. The bins contained 111 and 226 waveforms, respectively. The SSLIP method recovered a Moho depth of 56 km for both radii tested. We also considered a bin centered at (latitude = 33° N, longitude = 90° E), and radii of both 4° and 5°, but none of the results were deeper than 56 km depth. Therefore, careful bin definition and decreased bin radii can slightly improve resolution over that presented in Fig. 7. However, the improvement is small, and the SSLIP modelling approach gen-

erally averages small-scale features, as might be expected given the relatively large Fresnel zone of long-period SS reflections.

The SSLIP results are well correlated with the CRUST 2.0 and MDN results when compared directly (Fig. 8). To perform this comparison we averaged CRUST 2.0 and MDN values within 10° of the bin center, since these models report Moho depths at a finer scale than the 10° spacing of the SSLIP model. The MDN averages in Fig. 8(b) are not weighted by the standard deviation values supplied by this study, since large MDN depths are characterized by large standard deviations. Therefore, the weighted MDN average in deep Moho regions is systematically smaller than expected by CRUST 2.0 or the SSLIP model. Although this averaging scheme does not fully account for all of the expected resolution differences (such as the size of the SS bounce point Fresnel zone, see e.g. Shearer 1993), the depths are in reasonable agreement, with correlation coefficients of 0.82 (CRUST 2.0) and 0.74 (MDN). Averaged MDN and averaged CRUST 2.0 Moho depths are also well correlated in Asia (0.92). Although CRUST 2.0 and MDN have higher resolution than our SSLIP model, the good correlation of SSLIP with CRUST 2.0 and MDN is encouraging. In the future, a larger global database may enable better coverage outside Asia. More data will also enable smaller SSLIP bin radii, and thus somewhat increased lateral resolution.

We also experimented with other reference phases. For example, we stacked waveforms with bounce points at regions with crustal thicknesses from 35 to 45 km according to the CRUST 2.0 model. We convolved the resulting waveform with an inverse operator corresponding to 40 km crustal thickness, and used this new waveform as the reference phase to create the forward models for the inversion. The new reference phase closely resembles the oceanic stack. The inversion results are also similar to those of Fig. 7. Although
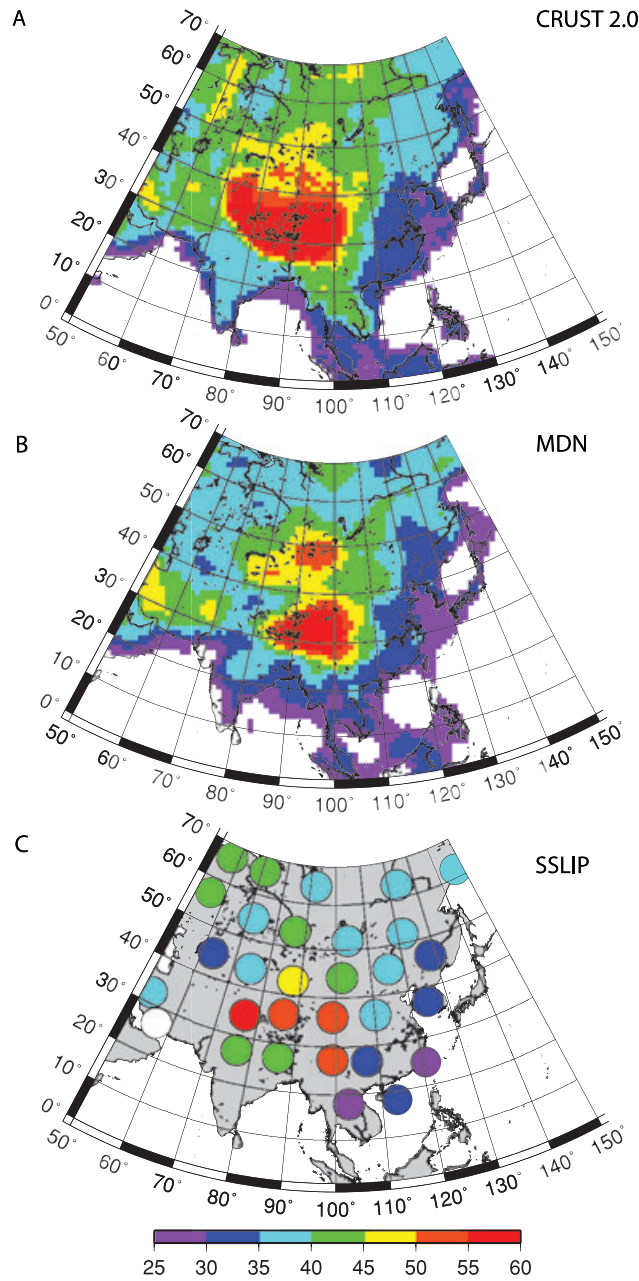
Figure 7. Moho depth results in Asia. (a) CRUST 2.0 Moho depth (Bassin *et al.* 2000). (b) MDN Moho depth (Meier *et al.* 2007). (c) SSLIP Moho depth. SSLIP depths are reported in locations determined to be continental in character using the binary ocean–continent test result in Fig. 4. SSLIP results are plotted at the locations of the bin centroids. The colour scale is saturated at 60 km. The CRUST 2.0 Moho reaches as deep as 75 km beneath Tibet, and MDN reaches 79 km.

an average of 2.5 km thicker, ∼75 per cent of the results from Asia are less than 5 km greater than inversions that use an oceanic reference stack. The result is within the estimated errors of the model presented here that used an oceanic reference phase. However, the variance of the model using this alternate reference phases is 15 per cent greater than the result using an oceanic reference phase, so the oceanic reference is preferred.
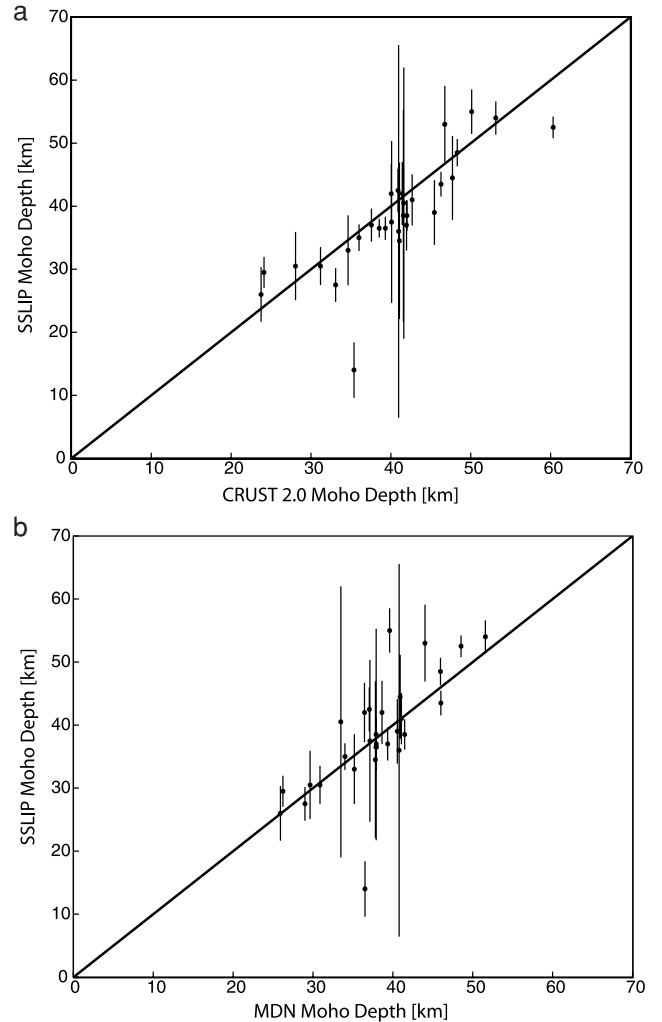

Figure 8. Direct comparison of SSLIP to other Moho results in Asia. (a) SSLIP compared to CRUST 2.0 Moho depths and (b) SSLIP compared to MDN Moho depths. CRUST 2.0 and MDN depths are calculated by averaging values within the 10° radii bin used to bin the SS waveforms. A 1:1 ratio is plotted as a black solid line for reference. Vertical lines represent SSLIP 95 per cent confidence limits determined by bootstrap resampling.

CONCLUSIONS

Lithospheric velocity discontinuities may be imaged using variations in the character of stacked SS waveforms. SS continent versus ocean waveform stacks are different primarily because of variations in Moho depth. Waveforms binned at regular intervals by bounce point demonstrate global variations in character dependent on the tectonic region of the bin and can resolve continents and oceans. SSLIP images variations in Moho depth across Asia that are in general agreement with models CRUST 2.0 and MDN, and the results are correlated at a lateral resolution of ∼10°. The SSLIP method may be useful in mapping crustal thickness in areas poorly sampled by other techniques.
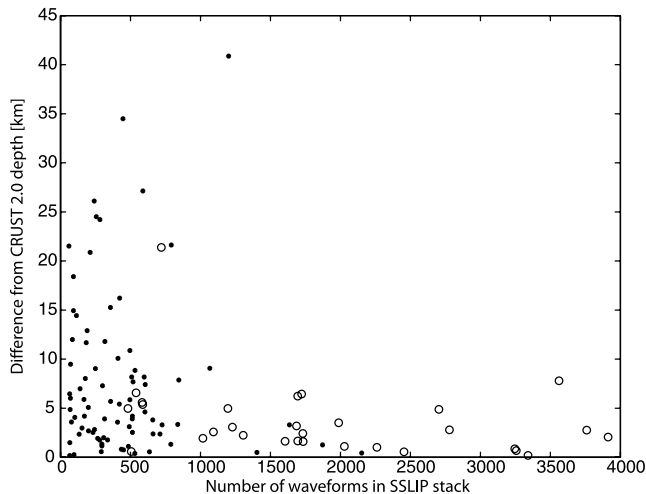
ACKNOWLEDGMENTS

Figure 9. Difference between SSLIP and CRUST 2.0 depth, compared to the number of waveforms stacked in each SSLIP bin. CRUST 2.0 Moho depths are calculated by averaging the model over the $10°$ radius bins used in the SSLIP model. The absolute values of the differences between CRUST 2.0 Moho depths and SSLIP Moho depths are compared to the number of bounce points in the SSLIP bins. All bins with continental character (Fig. 4) are plotted. Continental bins beneath Asia (Fig. 7) are plotted as open circles, while the rest of the continental bins are solid dots.

REFERENCES

Bassin, C., Laske, G. & Masters, T.G., 2000. The current limits of resolution for surface wave tomography in North America, *EOS, Trans. Am. geophys. Un.,* **81,** Fall Meet. Suppl., Abstract F897.

Behm, M., 2009. 3-D modelling of the crustal S-wave velocity structure from active source data: application to the Eastern Alps and the Bohemian Massif, *Geophys. J. Int.,* **179,** 265–278, doi:210.1111/j.1365–1246X.2009.04259.x

Bostock, M.G., 1998. Mantle stratigraphy and evolution of the Slave province, *J. geophys. Res.,* **103,** 21 183–121 200.

Bostock, M.G. & Rondenay, S., 1999. Migration of scattered teleseismic body waves, *Geophys. J. Int.,* **139,** 597–597.

Bump, H.A. & Sheehan, A.F., 1998. Crustal thickness variations accross the northern Tien Shan from teleseismic receiver functions, *Geophys Res. Lett.,* **25,** 1055–1058.

Chen, L., Zheng, T.Y. & Xu, W.W., 2006. A thinned lithospheric image of the Tanlu Fault Zone, eastern China: constructed from wave equation based receiver function migration, *J. geophys. Res.,* **111,** B09312, doi:09310.01029/02005JB003974.

Christensen, N.I. & Mooney, W.D., 1998. Seismic velocity structure and composition of the continental crust: a global view, *J. geophys. Res.,* **100,** 9761–9788.

Deuss, A. & Woodhouse, J., 2001. Seismic observations of splitting of the mid-transition zone discontinuity in Earth's mantle, *Science,* **294,** 354–357, doi:310.1126/science.1063524.

Flanagan, M.P. & Shearer, P.M., 1998. Global mapping of topography on transition zone velocity discontinuities by stacking SS precursors, *J. geophys. Res.,* **103,** 2673–2692.

Grad, M., Tiira, T. & ESC Working Group, 2009. The Moho depth map of the European Plate, *Geophys. J. Int.,* **176,** 276–292, doi:10.1111/j.1365-246X.2008.03919.x.

Gu, Y.J. & Dziewonski, A.M., 2002. Global variability of transition zone thickness, *J. geophys. Res.,* **107,** doi:10.1029/2001JB000489.

Hansen, S. & Dueker, K., 2009. P- and S-wave receiver function images of crustal imbrication beneath the Cheyenne Belt in Southeast Wyoming, *Bull. seism. Soc. Am.,* **99,** 1953–1961.

Jordan, T.H., 1981. Global tectonic regionalization for seismological data-analysis, *Bull. seism. Soc. Am.,* **71,** 1131–1141.

Kumar, P., Yuan, X.H., Kind, R. & Ni, J., 2006. Imaging the colliding Indian and Asian lithospheric plates beneath Tibet, *J. geophys. Res.,* **111,** B06308, doi:06310.01029/02005JB003930.

Lawrence, J.F. & Shearer, P.M., 2008. Imaging mantle transition zone thickness with SdS-SS finite-frequency sensitivity kernels, *Geophys. J. Int.,* **174,** 143–158, doi:110.1111/j.1365–1246X.2007.03673.x.

Liu, M., Mooney, W.D., Li, S., Okaya, N. & Detweiler, S., 2006. Crustal structure of the northeastern margin of the Tibetan plateau from the Songpan-Ganzi terrain to the Ordos basin, *Tectonophysics,* **420,** 253–266, doi:210.1016/j.tecto.2006.1001.1025.

Meier, U., Curtis, A. & Trampert, J., 2007. Global crustal thickness from neural network inversion of surface wave data, *Geophys. J. Int.,* **169,** 706–722, doi:710.1111/j.1365–1246X.2007.03373.x.

Mohorovičić, A., 1910. Potre of 8.X.1909, *Godisnje izvjesce zagrebackog meteoroloskog opservatorija,* **9,** 1–56.

MONA-LISA Working Group, 1997. MONA LISA–Deep seismic investigations of the lithosphere in the southeastern North Sea, *Tectonophysics,* **269,** 1–19.

Mooney, W.D., Laske, G. & Masters, T.G., 1998. CRUST 5.1: a global crustal model at 5 degrees x 5 degrees, *J. geophys. Res.,* **103,** 727–747.

Morozova, E.A., Morozov, I.B., Smithson, S.B. & Solodilov, L., 2000. Lithospheric boundaries and upper mantle heterogeneity beneath Russian Eurasia: evidence from the DSS profile QUARTZ, *Tectonophysics,* **329,** 333–344.

Morozova, E.A., Morozov, I.B., Smithson, S.B. & Solodilov, L.N., 1999. Heterogeneity of the uppermost mantle beneath Russian Eurasia from the ultra-long-range profile QUARTZ, *J. geophys. Res.,* **104,** 20329–20348.

Oda, H. & Ushio, T., 2007. Topography of the Moho and Conrad discontinuities in the Kyushu district, Southwest Japan, *J. Seismol.,* **11,** 221–223, doi:210.1007/s10950–10007-19049-z.

Oreshin, S., Kiselev, S., Vinnik, L., Prakasam, K.S., Rai, S., Makeyeva, L. & Savvin, Y., 2008. Crust and mantle beneath western Himalaya, Ladakh and western Tibet from integrated seismic data, *Earth planet. Sci. Lett.,* **271,** 75–87, doi:10.1016/j.epsl.2008.1003.1048.

Ozacar, A.A., Gilbert, H. & Zandt, G., 2008. Upper mantle discontinuity structure beneath East Anatolian Plateau (Turkey) from receiver functions, *Earth planet. Sci Lett.,* **269,** 426–434, doi:410.1016/j.epsl.2008.1002.1036.

Pavlenkova, G.A., Priestley, K. & Cipar, J., 2002. 2D model of the crust and uppermost mantle along rift profile, Siberian craton, *Tectonophysics,* **355** (1–4), 171–186, doi:10.1016/S0040-1951(02)00140-3.

Priestly, K.F., Jackson, J.A. & McKenzie, D.P., 2008. Lithospheric structure and deep earthquakes beneath India, the Himalaya and southern Tibet, *Geophys. J. Int.,* **172,** 345–362, doi:310.1111/j.1365–1246X.2007.03636.x.

Rychert, C.A. & Shearer, P.M., 2009. A global view of the lithosphere-asthenosphere boundary, *Science,* **324,** 495–498, doi:410.1126/science.1169754.

Rychert, C.A., Fischer, K.M. & Rondenay, S., 2005. A sharp lithosphere-asthenosphere boundary imaged beneath eastern North America, *Nature,* **436,** 542–545, doi:510.1038/nature03904.

Rychert, C.A., Rondenay, S. & Fischer, K.M., 2007. P-to-S and S-to-P imaging of a sharp lithosphere–asthenosphere boundary beneath eastern North America, *J. geophys. Res.,* **112,** B08314, doi:08310.01029/02006JB004619.

Rychert, C.A., Shearer, P.M. & Fischer, K.M., 2009. Scattered wave imaging of the lithosphere–asthenosphere boundary, *Lithosphere,* in press, doi:10.1016/j.lithos.2009.12.006.

Schutt, D.L., Dueker, K. & Yuan, H., 2008. Crust and upper mantle velocity structure of the Yellowstone hot spot and surroundings, *J. geophys. Res.,* **113,** doi:10.1029/2007JB005109.

Shapiro, N. & Ritzwoller, M., 2002. Monte-Carlo inversion for a global shear-velocity model of the crust and upper mantle, *Geophys. J. Int.,* **151,** 88–105.

Shearer, P.M., 1991. Constraints on Upper Mantle Discontinuities from Observations of Long-Period Reflected and Converted Phases. *J. geophys. Res.,* **96**(B11), 18147–18182.

Shearer, P.M., 1993. Global mapping of upper-mantle reflections from long-period SS precursors. *Geophys. J. Int.,* **115**(3), 878–904.

Shearer, P.M., 1996. Transition zone velocity gradients and the 520-km discontinuity, *J. geophys. Res.,* **101**, 3053–3066.

Steer, D.N., Knapp, J.H., Brown, L.D., Echtler, H.P., Brown, D.L. & Berzin, R., 1998. Deep structure of the continental lithosphere in an unextended orogen: an explosive-source seismic reflection profile in the Urals (Urals Seismic Experiment and Integrated Studies (URSEIS 1995)), *Tectonics,* **17**, 143–157.

Zhang, Z. & Wang, Y., 2007. Crustal structure and contact relationship revealed from deep seismic sounding data in South China, *Phys. Earth planet. Inter.,* **165**, 114–126, doi:110.1016/j.pepi.2007.1008.1005.

Zhang, Z., Yanghua, W., Chen, Y., Houseman, G.A., Tian, X., Wang, E. & Teng, J., 2009. Crustal structure across Longmenshan fault belt from passive source seismic profiling, *Geophys. J. Int.,* **36**, doi:10.1029/2009GL039580.

Zhou, Y., Dahlen, F.A., Nolet, G. & Laske, G., 2005. Finite-frequency effects in global surface-wave tomography, *Geophys. J. Int.,* **163**, 1087–1111, doi:1010.1111/j.1365–1246X.2005.02780.x.

Zhu, L. & Helmberger, D.V., 1998. Moho offset across the northern margin of the Tibetan Platesu, *Science,* **21**, 1170–1172, doi:1110.1126/science.1281.5380.1170.

Zhu, L. & Kanamori, H., 2000. Moho depth variation in southern California from teleseismic receiver functions, *J. geophys. Res.,* **105**, 2969–2980.